

Computation of Casimir Interactions between Arbitrary 3D Objects with Arbitrary Material Properties

M. T. Homer Reid^{1,2}, Jacob White^{2,3}, and Steven G. Johnson^{2,4}

¹*Department Of Physics, Massachusetts Institute of Technology, Cambridge, MA 02139, USA*

²*Research Laboratory of Electronics, Massachusetts Institute of Technology, Cambridge, MA 02139, USA*

³*Department of Electrical Engineering and Computer Science,
Massachusetts Institute of Technology, Cambridge, MA 02139, USA*

⁴*Department Of Mathematics, Massachusetts Institute of Technology, Cambridge, MA 02139, USA*

(Dated: October 21, 2011)

We extend a recently introduced method for computing Casimir forces between arbitrarily-shaped metallic objects [M. T. H. Reid *et al.*, Phys. Rev. Lett. **103** 040401 (2009)] to allow treatment of objects with arbitrary material properties, including imperfect conductors, dielectrics, and magnetic materials. Our original method considered electric currents on the surfaces of the interacting objects; the extended method considers both electric *and* magnetic surface current distributions, and obtains the Casimir energy of a configuration of objects in terms of the interactions of these effective surface currents. Using this new technique, we present the first predictions of Casimir interactions in several experimentally relevant geometries that would be difficult to treat with any existing method. In particular, we investigate Casimir interactions between dielectric nanodisks embedded in a dielectric fluid; we identify the threshold surface–surface separation at which finite-size effects become relevant, and we map the rotational energy landscape of bound nanoparticle diclusters.

PACS numbers: 03.70.+k, 12.20.-m, 42.50.Lc, 03.65.Db

Rapid progress in experimental Casimir physics [1] has created a demand for theoretical tools that can predict Casimir forces and torques on bodies with realistic material properties, configured in experimentally relevant geometries. Techniques for computing Casimir interactions have traditionally fallen into two categories [2]. In the *scattering* approach [3], the Casimir energy is obtained from spectral properties of the classical electromagnetic (EM) scattering matrix of the geometry; this method leads to rapidly convergent and even *analytically* tractable [4] formulae for certain highly symmetric geometries in which a special choice of coordinates leads to a simple form for the scattering matrix, but is less readily applicable to objects of general asymmetric shapes. In the alternative *numerical stress-tensor* (ST) approach [5], the Casimir force and torque on a compact body are obtained by numerically integrating the (thermally and quantum-mechanically averaged) Maxwell ST over a bounding surface surrounding that body, with the value of the ST at each spatial point obtained by solving a classical EM scattering problem. The ST method has the virtue of flexibility, as almost any of the myriad existing methods for computational EM packages may be applied off-the-shelf to solve scattering problems for arbitrary geometries and materials, but the ST integration adds a layer of conceptual and computational complexity.

In recent work [6], we have introduced a new method for Casimir computations that combines the best features of the scattering and stress-tensor approaches. Our *surface-current* technique discretizes the surfaces of interacting objects into small surface patches (Fig. 1)—thus retaining the full flexibility of the numerical ST approach in handling arbitrarily complex, asymmetric

geometries—but bypasses the unwieldy ST integration by obtaining the Casimir energy directly from spectral properties of a matrix describing the interactions of *surface currents* on the discretized object surfaces—thus mirroring the conceptual directness of the scattering approach, dramatically improving computational effi-

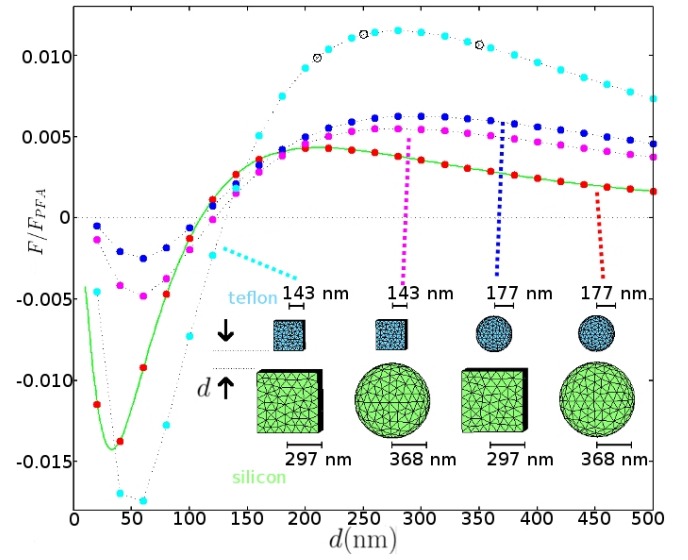


FIG. 1. Casimir force between silicon and teflon spheres and cubes immersed in ethanol, normalized by the PFA predictions (see text). For the sphere-sphere case, the solid circles represent data computed using the methods described in this paper, while the thick solid line reproduces data from Ref. [7]. For the other three cases, the solid and hollow circles represent data computed using the methods described in this paper, and the dotted lines are a guide to the eye.

ciency for moderate-size problems where dense linear algebra is applicable, and establishing a connection to the equivalent-surface-current method of classical EM [8].

The technique discussed in [6] was limited to the case of perfect-metal bodies in vacuum. In this paper we extend the method to allow treatment of materials with *arbitrary* frequency-dependent (but spatially constant) permittivity ϵ and permeability μ . A thorough description of our extended formulation will be provided elsewhere [9]; here we present a brief overview of our method and demonstrate its use in predicting Casimir interactions in systems that would be difficult to treat by any other method.

Casimir Interactions from Surface Currents. The Casimir energy of a collection of objects is given quite generally by an expression of the form [10]

$$\mathcal{E} = -\frac{\hbar}{2\pi} \int_0^\infty d\xi \log \frac{\mathcal{Z}(\xi)}{\mathcal{Z}_\infty(\xi)} \quad (1)$$

where the partition function for the electromagnetic field at imaginary frequency ξ is

$$\mathcal{Z}(\xi) = \int [\mathcal{D}\mathbf{A}]_c e^{-\frac{1}{2} \int \mathbf{A}(\xi, \mathbf{x}) \cdot \mathbf{G}^{-1}(\xi, \mathbf{x}, \mathbf{x}') \cdot \mathbf{A}(\xi, \mathbf{x}')} d\mathbf{x} d\mathbf{x}'; \quad (2)$$

here \mathbf{G} is the (gauge-fixed) photon propagator, and the notation $[\dots]_c$ indicates that this is a *constrained* path integral, in which the path integration ranges only over field configurations \mathbf{A} that satisfy the boundary conditions in the presence of the interacting objects. (\mathcal{Z}_∞ in (1) is \mathcal{Z} with all objects removed to infinite separations.)

Although the exponent in (2) is only quadratic in the integration variables, the implicit constraint in the integration measure prevents direct evaluation of the path integral. We obtain a more tractable expression by representing the constraints on the \mathbf{A} field *explicitly* via functional δ functions [11, 12]. Consider a single point \mathbf{x} on the surface of an object in our geometry. The boundary conditions at \mathbf{x} are that the components of \mathbf{E} and \mathbf{H} tangential to the object surface are continuous as we pass from the interior to the exterior of the object at \mathbf{x} :

$$\mathbf{E}_\parallel^{\text{in}}(\mathbf{x}) = \mathbf{E}_\parallel^{\text{out}}(\mathbf{x}), \quad \mathbf{H}_\parallel^{\text{in}}(\mathbf{x}) = \mathbf{H}_\parallel^{\text{out}}(\mathbf{x}).$$

We introduce two 2-dimensional δ functions that impose these constraints at \mathbf{x} :

$$\begin{aligned} \delta(\mathbf{E}_\parallel^{\text{in}}(\mathbf{x}) - \mathbf{E}_\parallel^{\text{out}}(\mathbf{x})) &= \int_{-\infty}^\infty \int_{-\infty}^\infty \frac{dK_1 dK_2}{(2\pi)^2} e^{i\mathbf{K} \cdot [\mathbf{E}^{\text{in}}(\mathbf{x}) - \mathbf{E}^{\text{out}}(\mathbf{x})]} \\ \delta(\mathbf{H}_\parallel^{\text{in}}(\mathbf{x}) - \mathbf{H}_\parallel^{\text{out}}(\mathbf{x})) &= \int_{-\infty}^\infty \int_{-\infty}^\infty \frac{dN_1 dN_2}{(2\pi)^2} e^{i\mathbf{N} \cdot [\mathbf{H}^{\text{in}}(\mathbf{x}) - \mathbf{H}^{\text{out}}(\mathbf{x})]} \end{aligned}$$

where we may think of the Lagrange multipliers \mathbf{K} and \mathbf{N} as two-component vectors living in the tangent space to the object surface at \mathbf{x} . Aggregating the corresponding δ functions for *all* points \mathbf{x} on all object surfaces, we obtain an explicit *functional* δ function constraining the electromagnetic field to satisfy the boundary conditions:

$$\delta[\mathbf{A}] = \int \mathcal{D}\mathbf{K} \int \mathcal{D}\mathbf{N} e^{\oint \{ i\mathbf{K} \cdot \mathcal{L}^E \mathbf{A} + i\mathbf{N} \cdot \mathcal{L}^H \mathbf{A} \} d\mathbf{x}} \quad (3)$$

where the integration in the exponent is over the surfaces of all objects in our geometry, the path integrations range over all possible tangential vector fields $\mathbf{K}(\mathbf{x}), \mathbf{N}(\mathbf{x})$ on the object surfaces, and $\mathcal{L}^E, \mathcal{L}^H$ are differential operators that act on \mathbf{A} to yield \mathbf{E} and \mathbf{H} . Because \mathbf{K} and \mathbf{N} respectively enforce the boundary conditions on the *electric* and *magnetic* fields, it is tempting to interpret these tangential vector fields as *electric* and *magnetic* surface current distributions on the surfaces of the interacting objects. Effective surface current distributions of this sort are ubiquitous in equivalence-principle techniques for EM field computation [8] and form the basis of the boundary-element method of computational EM [13].

Inserting the explicit constraint (3) into the path integral (2) allows us to relax the implicit constraint $[\dots]_c$, whereupon the path integral over the \mathbf{A} field may be performed analytically:

$$\begin{aligned} \mathcal{Z}(\xi) &= \int \mathcal{D}\mathbf{A} \mathcal{D}\mathbf{K} \mathcal{D}\mathbf{N} e^{-\frac{1}{2} \int \mathbf{A} \mathbf{G}^{-1} \mathbf{A} + i \oint \mathbf{A} \cdot [\mathcal{L}^E \mathbf{K} + \mathcal{L}^H \mathbf{N}]} \\ &\sim \int \mathcal{D}\mathbf{K} \mathcal{D}\mathbf{N} \exp\{-S_\xi[\mathbf{K}, \mathbf{N}]\} \end{aligned} \quad (4)$$

where \sim denotes equality up to constant factors that cancel in the ratio in (1), and where the effective action

$$S_\xi[\mathbf{K}, \mathbf{N}] = \oint \left\{ \begin{pmatrix} \mathbf{K} \\ \mathbf{N} \end{pmatrix}^T \cdot \begin{pmatrix} \mathcal{L}^E \mathbf{G} \mathcal{L}^E & \mathcal{L}^E \mathbf{G} \mathcal{L}^H \\ \mathcal{L}^H \mathbf{G} \mathcal{L}^E & \mathcal{L}^H \mathbf{G} \mathcal{L}^H \end{pmatrix} \cdot \begin{pmatrix} \mathbf{K} \\ \mathbf{N} \end{pmatrix} \right\} d\mathbf{x}$$

describes the interactions of electric and magnetic surface currents on the bodies of the interacting objects. The frequency-dependent material parameters $\epsilon(\xi), \mu(\xi)$ of all interacting objects, and of the medium in which they are embedded, enter into S_ξ through $\mathcal{L}^E, \mathcal{L}^H$, and \mathbf{G} .

Discretization. To evaluate (4) for a given collection of objects, we now proceed as in [6] by discretizing the surfaces of the objects into small planar triangles [14]. We introduce a set [15] of localized vector-valued basis functions $\{\mathbf{f}_\alpha\}$ and approximate the surface currents $\mathbf{K}(\mathbf{x}), \mathbf{N}(\mathbf{x})$ as expansions in the finite set $\{\mathbf{f}_\alpha\}$:

$$\mathbf{K}(\mathbf{x}) \approx \sum_\alpha K_\alpha \mathbf{f}_\alpha(\mathbf{x}), \quad \mathbf{N}(\mathbf{x}) \approx \sum_\alpha N_\alpha \mathbf{f}_\alpha(\mathbf{x}).$$

The functional integral in (4) becomes a finite-dimensional Gaussian integral,

$$\begin{aligned} \int \mathcal{D}\mathbf{K} \mathcal{D}\mathbf{N} e^{-S_\xi[\mathbf{K}, \mathbf{N}]} &\sim \int \prod dK_\alpha dN_\alpha e^{-\binom{K}{N} \cdot \mathbf{M}(\xi) \cdot \binom{K}{N}} \\ &\sim [\det \mathbf{M}(\xi)]^{-1/2} \end{aligned} \quad (5)$$

and, inserting into (1), the Casimir energy becomes

$$\mathcal{E} = \frac{\hbar}{2\pi} \int_0^\infty d\xi \log \frac{\det \mathbf{M}(\xi)}{\det \mathbf{M}_\infty(\xi)} \quad (6)$$

while differentiating with respect to the position of an object gives the Casimir force on that object:

$$\mathcal{F}_i = -\frac{\hbar}{2\pi} \int_0^\infty d\xi \text{Tr} \left\{ \mathbf{M}^{-1} \cdot \frac{\partial \mathbf{M}}{\partial \mathbf{x}_i} \right\}. \quad (7)$$

The matrix \mathbf{M} describes interactions among the effective electric and magnetic surface currents. More specifically, each pair of localized basis functions ($\mathbf{f}_\alpha, \mathbf{f}_\beta$) corresponds to a 2×2 block of \mathbf{M} of the form

$$\mathbf{M}_{\alpha\beta} = \begin{pmatrix} \langle \mathbf{f}_\alpha | \mathbf{G}^{\text{EE}} | \mathbf{f}_\beta \rangle & \langle \mathbf{f}_\alpha | \mathbf{G}^{\text{EM}} | \mathbf{f}_\beta \rangle \\ \langle \mathbf{f}_\alpha | \mathbf{G}^{\text{ME}} | \mathbf{f}_\beta \rangle & \langle \mathbf{f}_\alpha | \mathbf{G}^{\text{MM}} | \mathbf{f}_\beta \rangle \end{pmatrix}$$

where e.g. \mathbf{G}^{ME} is a dyadic Green's function representing the magnetic field due to a point electric dipole source.

Comparison to the BEM. The matrix \mathbf{M} has precisely the same form as the matrix that arises in the boundary-element method (BEM) for electromagnetic scattering problems [13]. Indeed, once we have implemented the computational machinery needed to evaluate (7), we could alternatively use this same machinery to compute Casimir forces in a different way—namely, by numerically integrating the ST over a bounding surface, with the value of the ST at each spatial quadrature point obtained by solving a BEM scattering problem [16]. This procedure would entail solving linear systems $\mathbf{M} \cdot \mathbf{X} = \mathbf{B}$ for multiple vectors \mathbf{B} , which in practice would be handled by first decomposing \mathbf{M} into triangular factors. Such a factorization step is also required for numerical evaluation of the determinant or trace expressions in (6–7). However, in our formulation, this factorization step is *all* that is required, with the Casimir energy and force then obtained immediately from the simple relations (6–7); in contrast, the ST method requires extensive pre- and post-processing, in addition to the factorization of the BEM matrix, to evaluate the ST integral. Thus, in addition to the conceptual simplicity of our equations (6–7) as compared to the ST formulation, our method is significantly more computationally efficient than the ST approach, at least as long as we consider problems of moderate size ($N \equiv \dim \mathbf{M} \lesssim 10^4$), for which direct linear-algebra methods are feasible.

As an explicit demonstration of this computational advantage, the three points represented by hollow circles on the cube–cube data curve in Figure 1 were computed by the ST-integration method using our BEM code. The resulting force predictions agree with the predictions of (7), but consume some 12–24 times more CPU time.

Moreover, although here we derived our equation (7) in the context of the scattering approach to Casimir physics, the same equation can alternatively be shown to follow directly from an application of the BEM to stress-tensor Casimir computations, with the spatial integral evaluated *analytically*. Full details of these two complementary derivations will be presented in [9].

Applications. We now use our extended method to predict Casimir interactions in a number of new systems that would be difficult to treat with any other method.

Attractive and repulsive Casimir forces between silicon and teflon spheres and cubes immersed in ethanol. Ref. [7], using the methods of Ref. [4], predicted Casimir

forces between spheres and slabs composed of various materials and suspended in ethanol. Figure 1 validates our method by using it to reproduce the results of Ref. [7] for the Casimir force between teflon and (undoped) silicon spheres, then extends these results by plotting Casimir forces between spheres and cubes of the same material properties (with the cubes sized to have the same volume as the corresponding spheres). For each geometry, we plot the ratio of the computed Casimir force to the force predicted by the perfect-metal proximity force approximation (PFA) for that geometry; since the PFA always predicts an attractive force, a positive (negative) ratio implies an attractive (repulsive) Casimir force. It is interesting that all four geometries exhibit a repulsive–attractive force crossover at approximately the same surface–surface separation distance.

Finite-size effects in nanoparticle dusters. Ref. [7] predicted Casimir forces between dielectric slabs, of infinite cross-sectional-area, embedded in ethanol. It is interesting to ask how these predictions are modified for *finite* slabs (discs). Figure 2 plots the PFA-normalized Casimir force between pairs of puck-shaped nanoparticles, one composed of polystyrene and the other of doped silicon, immersed in ethanol. For comparison, the dotted curves indicate the (PFA-normalized) force between pairs of infinite slabs of the same materials. For small values of the surface–surface separation d , the normalized puck-puck force tends to the slab-slab limit, but finite-size effects cause the curves to deviate beyond separations of

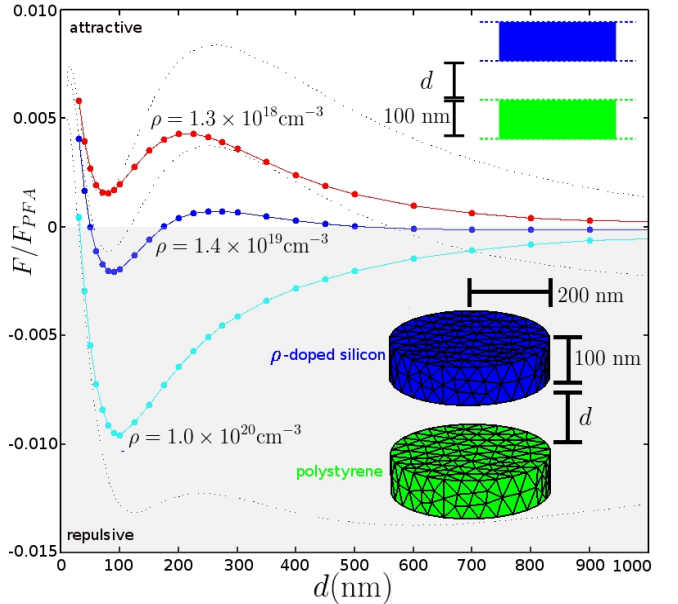


FIG. 2. Casimir force between puck-shaped polystyrene and doped-silicon (dopant density ρ) nanoparticles immersed in ethanol. The dotted curves indicate the force on *slabs* of the same materials and thickness but infinite cross-sectional area [7]. (Material properties are taken from Ref. [7].)

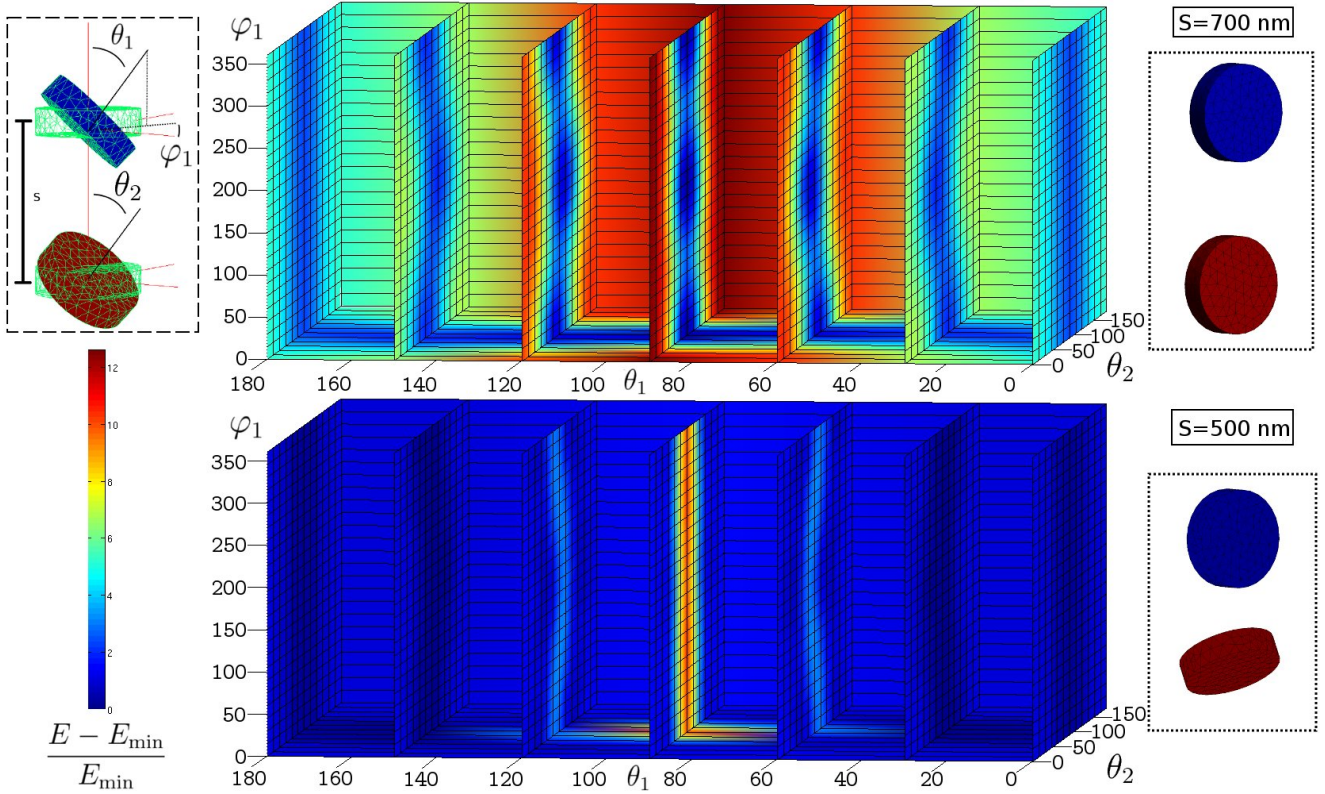


FIG. 3. (Color) Rotational stability of hockey-puck shaped nanoparticles suspended in ethanol. One nanoparticle is composed of polystyrene, and the other of silicon with a dopant concentration of $1.4 \cdot 10^{19} \text{ cm}^{-3}$ (corresponding to the middle curve in the previous plot). We fix the centers of the particles at center–center separations of $S = \{500, 700\} \text{ nm}$ allow them to rotate about their centers. The minimum-energy configurations are depicted in the insets at right. (All angles are measured in degrees.)

$d \sim R/2$ (with R the puck radius).

Rotational stability of dielectric nanoparticles. For the nanoparticle pair corresponding to the intermediate curve in Figure 2 (dopant density of $1.4 \cdot 10^{19} \text{ cm}^{-3}$ for the silicon nanoparticle), we now fix the centroids of the nanoparticles and plot the Casimir energy (Figure 3) as a function of rotation angles (see the inset of Figure 3) for two centroid–centroid separation distances S of 700 and 500 nm. The slight shift in the value of S changes the stable equilibrium (right).

Acknowledgements. We are grateful to A. Rodriguez for providing the raw data from Ref. [7]. The authors are grateful for support from the Singapore-MIT Alliance Computational Engineering flagship research program.

and J. Wagner, Phys. Rev. Lett., **101**, 160402 (2008)

- [3] S. J. Rahi, T. Emig, N. Graham, R. L. Jaffe, and M. Kardar, Phys. Rev. D, **80**, 085021 (2009).
- [4] T. Emig, N. Graham, R. L. Jaffe, and M. Kardar, Phys. Rev. Lett., **99**, 170403 (2007).
- [5] A. W. Rodriguez, M. Ibanescu, D. Iannuzzi, J. D. Joannopoulos, and S. G. Johnson, Phys. Rev. A, **76**, 032106 (2007).
- [6] M. T. H. Reid, A. W. Rodriguez, J. White, and S. G. Johnson, Phys. Rev. Lett., **103**, 040401 (2009).
- [7] A. W. Rodriguez, A. P. McCauley, D. Woolf, F. Capasso, J. D. Joannopoulos, and S. G. Johnson, Phys. Rev. Lett., **104**, 160402 (2010).
- [8] R. F. Harrington, *Time-Harmonic Electromagnetic Fields* (Wiley-IEEE Press, 2001) chapter 3.
- [9] M. T. H. Reid, to appear.
- [10] We work here at zero temperature T ; the extension to finite T is straightforward and will be presented in [9].
- [11] M. Bordag, D. Robaschik, and E. Wieczorek, Ann. Phys., **165**, 192 (1985).
- [12] H. Li and M. Kardar, Phys. Rev. Lett., **67**, 3275 (1991).
- [13] L. N. Medgyesi-Mitschang, J. M. Putnam, and M. B. Gedera, J. Opt. Soc. Am. A, **11**, 1383 (1994).
- [14] C. Geuzaine and J.-F. Remacle, Int. J. Numer. Meth. Eng., **79**, 1309 (2009).
- [15] S. M. Rao, D. R. Wilton, and A. W. Glisson, IEEE Trans. Antennas Propagat., **AP-30**, 409 (1982).
- [16] J. L. Xiong, M. S. Tong, P. Atkins, and W. C. Chew,

Phys. Lett. A, **374**, 2517 (2010).